



Innovative functionalization of Vulcan XC-72 with Ru organometallic complex: Significant enhancement in catalytic activity of Pt/C electrocatalyst for the methanol oxidation reaction (MOR)



A.A. Siller-Ceniceros ^a, M.E. Sánchez-Castro ^{a,b}, D. Morales-Acosta ^c, J.R. Torres-Lubian ^c, E. Martínez G. ^d, F.J. Rodríguez-Varela ^{a,b,*}

^a Nanociencias y Nanotecnología, Cinvestav Unidad Saltillo, Av. Industria Metalúrgica 1062, Parque Industrial Ramos Arizpe, Ramos Arizpe, Coah. C.P. 25900, Mexico

^b Sustentabilidad de los Recursos Naturales y Energía, Cinvestav Unidad Saltillo, Mexico

^c CONACYT-Centro de Investigación en Química Aplicada, Blvd. Enrique Reyna No. 140, Saltillo, Coah. C.P. 25294, Mexico

^d Centro de Investigación en Materiales Avanzados, S.C. Alianza Norte 202, PIIT, Carretera Monterrey-Aeropuerto Km. 10, Apodaca, NL C.P. 66628, Mexico

ARTICLE INFO

Article history:

Received 14 October 2016

Received in revised form 29 January 2017

Accepted 3 March 2017

Available online 6 March 2017

Keywords:

Surface functionalization

Vulcan support

Ru organometallic complex

Pt nanocatalysts

Methanol Oxidation Reaction

ABSTRACT

In this work, a novel procedure to enhance the catalytic activity of Pt/C for the MOR by promoting surface Pt–Ru metal interactions is proposed. Vulcan is functionalized with home-prepared ruthenium (II) arene compound $[(\eta^6\text{-C}_6\text{H}_5\text{OCH}_2\text{CH}_2\text{OH})\text{RuCl}_2]_2$ (*Ru-dim*) and labeled $\text{C}_{\text{Ru-dim}}$. Then, $\text{Pt/C}_{\text{Ru-dim}}$ is synthesized with the polyol method. Also, Vulcan functionalized with $\text{RuCl}_3 \cdot \text{XH}_2\text{O}$ (*Ru-com*) and non-functionalized Vulcan are used to prepare $\text{Pt/C}_{\text{Ru-com}}$ and Pt/C, respectively. The results show that functionalization with *Ru-dim* maintains the electronic sp^2 hybridization of the graphitic segment of Vulcan. Physicochemical characterization strongly suggests the formation of Pt–Ru alloyed phases at $\text{Pt/C}_{\text{Ru-dim}}$: XRD shows about 50% Ru alloyed, while XPS indicates a shift of 0.32 eV toward higher BE of Pt^0 . Such Pt–Ru interactions enhance the performance of $\text{Pt/C}_{\text{Ru-dim}}$ for the MOR in acid media by reaching a current density of 45.0 mA cm^{-2} , two-fold increase compared to Pt/C. Moreover, the on-set potential of 0.25 V determined for $\text{Pt/C}_{\text{Ru-dim}}$ is 0.14 V more negative relative to Pt/C. In summary, $\text{Pt/C}_{\text{Ru-dim}}$ shows enhanced catalytic properties for Direct Methanol Fuel Cells (DMFCs) applications.

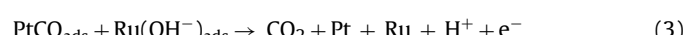
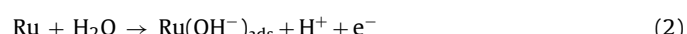
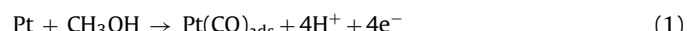
© 2017 Elsevier B.V. All rights reserved.

1. Introduction

DMFCs are high-energy density power devices, with relatively low environmental impact. For instance, DMFCs do not produce unburned hydrocarbons, nitrogen oxides, sulphur dioxide and particulates that are formed from the burning of fossil fuels in internal combustion engines. The use of methanol simplifies their implementation, since the infrastructure required for transportation and storage of the liquid fuel can be easily put into operation from existing installations [1]. Yet, it is well known that the MOR is rather complex, both in acid and alkaline media [2]. Platinum is commonly used as anode catalyst to promote this electrochemical reaction. However, besides being an expensive and scarce noble metal, it

becomes irreversibly poisoned by chemisorbed CO_{ads} , one of the main reaction intermediates from the MOR.

Forming alloys with other metals (e.g., Ru) not only increases the catalytic activity of binary Pt-catalysts toward the MOR, but also their electrochemical stability as well as their tolerance to CO_{ads} [3–6]. The enhanced catalytic activity of Pt–Ru/Carly alloys for the MOR has been attributed to the ligand effect and the bifunctional mechanism [4,7]. In the latter, the Ru atoms adsorb/desorb OH^- species at more negative potentials than Pt, catalyzing the oxidation of CO_{ads} to CO_2 , as can be described by the following reactions [7]:



Pt–Ru interactions are commonly achieved by simultaneously reducing, with the aid of a suitable chemical agent, the Pt and Ru precursors to form alloyed Pt–Ru nanoparticles anchored on a carbon support [8–11].

* Corresponding author at: Nanociencias y Nanotecnología, Cinvestav Unidad Saltillo, Av. Industria Metalúrgica 1062, Parque Industrial Ramos Arizpe, Ramos Arizpe, Coah. C.P. 25900, Mexico.

E-mail address: javier.varela@cinvestav.edu.mx (F.J. Rodríguez-Varela).

Meanwhile, in recent years the concept of functionalization of carbon structures has increasingly gained attention, because the morphological and electrocatalytical properties of fuel cell nanocatalysts can be enhanced by the surface modification of the supports [12–14]. A synergistic effect between the metallic catalyst and the functional groups on the support has been identified as one of the main factors for the enhancement in catalytic activity [15]. Even more, it has been proposed that oxygenated functional groups promote an increase in performance of Pt/C catalysts for the MOR [15]. The same synergistic effect has been reported for Pt–Ru/C alloys, where the use of Vulcan containing more oxygenated species increased the catalytic activity for the MOR [16]. Similar positive effects on other carbonaceous supports such as Ordered Mesoporous Carbon, Carbon Nanotubes and Graphene are reported elsewhere [17–19].

As a detailed review of the literature would reveal, a wide variety of chemical agents have been proposed to achieve the surface modification of carbon supports [20–24]. Nevertheless, no information has been found related to the surface functionalization of Vulcan with organometallic compounds to be used as support. The purpose of such approximation is to take advantage of the metallic phases in the organometallic chemical structure, aiming to form Pt–M alloys via *in situ* reactions during the reduction of platinum precursors. For instance, the metallic Ru phase in a ruthenium compound-functionalized Vulcan may interact with the Pt salt during the synthesis of Pt/C catalysts to promote Pt–Ru alloyed phases. In addition oxygenated, carbonyl and/or carboxyl functional groups can also be produced from the chemical surface reaction.

In this study, a novel methodology to enhance the catalytic activity of Pt/C electrocatalysts for the MOR is proposed. In a first stage, Vulcan is functionalized with home-obtained *Ru-dim*, slightly modifying a route described elsewhere [25–27]. Then, the modified $C_{Ru\text{-dim}}$ is used as support of the Pt/ $C_{Ru\text{-dim}}$ electrocatalyst synthesized via the polyol method [28]. The novelty of this methodology aimed to increase the catalytic activity for the MOR, is that three goals are searched: i) to promote the formation of alloyed Pt–Ru phases; ii) to form surface functional groups; iii) to efficiently attach Pt nanoparticles well dispersed on the support. For comparison, Vulcan modified with commercial $RuCl_3 \cdot XH_2O$, as well as non-functionalized Vulcan, are employed as supports to fabricate Pt/ $C_{Ru\text{-com}}$ and Pt/C, respectively. This approach differs from that implemented elsewhere, at which the bimetallic $CpRu(PPh_3)(\mu\text{-Cl})(\mu\text{-dppm})PtCl_2$ compound having Pt–Ru metallic phases and no carbon support has been proposed as electrocatalyst for the MOR [29]. Moreover, unlike the proposed Organometallic Fuel Cells (OMFCs) [30,31], this work focuses only on the generation of energy from the oxidation of methanol, as in a DMFC configuration. Nonetheless, it is not discarded that $C_{Ru\text{-dim}}$ can selectively participate in the production of chemicals and energy at given experimental conditions in alkaline OMFCs.

The electrocatalysts are characterized by XRD, SEM-EDS, HR-TEM and XPS. Even if the specific type of Pt–Ru interactions at Pt/ $C_{Ru\text{-dim}}$ is yet to be ascertain, this study strongly suggests that an alloyed Pt–Ru electrocatalyst is obtained. This is confirmed by the electrochemical characterization that demonstrates a considerably higher catalytic activity for the MOR and tolerance to CO_{ads} of Pt/ $C_{Ru\text{-dim}}$, compared to Pt/ $C_{Ru\text{-com}}$ and Pt/C.

2. Experimental

2.1. Materials

Vulcan XC-72 was obtained from Cabot Corp. Ruthenium chloride ($RuCl_3 \cdot XH_2O$), ethylene glycol ($C_2H_6O_2$), 1-methoxy-1,4-cyclohexadiene ($C_6H_7OCH_3$), ethanol (C_2H_5OH), methanol

(CH_3OH), ethylic ether ($((C_2H_5)_2O)$, benzophenone ($C_{13}H_{10}O$), iodine (I_2), magnesium (Mg), tetrahydrofuran (C_4H_8O), deuterated water (D_2O), chloroplatinic acid hexahydrate ($H_2PtCl_6 \cdot XH_2O$), Nafion solution (5 wt.%), sulfuric acid (H_2SO_4), nitric acid (HNO_3), sodium hydroxide ($NaOH$), were purchased from Sigma Aldrich. Deionized water was acquired from Jelmeck. pH calibration standards (4.00 ± 0.01 , 7.00 ± 0.01 and 10.00 ± 0.01) were obtained from Thermo Fisher Scientific. Ultra high purity Argon (Ar), carbon monoxide (CO), gas and liquid nitrogen ($N_{2(g)}$ and $N_{2(l)}$), were purchased from Infra.

2.2. Synthesis of Ru-dim

The organometallic compound $[(\eta^6-C_6H_5OCH_2CH_2OH)RuCl_2]_2$ (*Ru-dim*) was obtained following the methodology reported in [25], with slight modifications as follows: methoxy-1,4-cyclohexadiene (2.25 mL, 19.2 mmol) was added to a 1,2-ethanediol solution (15 mL) of ruthenium trichloride trihydrate (1.0 g, 3.82 mmol), followed by heating at $120^\circ C$ for 3 h. Yield: 702 mg, i.e., 59.26%.

2.3. Synthesis of $C_{Ru\text{-dim}}$ and $C_{Ru\text{-com}}$

$C_{Ru\text{-dim}}$ was obtained from the functionalization of Vulcan XC-72 with the organometallic compound, starting from a *Ru-dim*:Vulcan molar ratio of 1:10 [32], as follows: 104.16 mg (0.168 mmol) of *Ru-dim* and 20 mg (1.68 mmol) of Vulcan were stirred in 8 mL of THF under Ar atmosphere and refluxing conditions for 24 h at $130^\circ C$. The black solution generated was transferred into a Schlenk tube, filtered through a cannula, washed with dried THF and finally dried in vacuum for 12 h, resulting in a black/reddish powder.

$C_{Ru\text{-com}}$ was obtained following the same procedure, starting from 43.93 mg (0.168 mmol) of $RuCl_3 \cdot XH_2O$ and 20 mg of Vulcan, resulting in a black powder. Additionally, non-functionalized Vulcan (C) was used without further treatment.

2.4. Synthesis of Pt/C electrocatalysts

The 20 wt.% Pt/ $C_{Ru\text{-dim}}$, Pt/ $C_{Ru\text{-com}}$ and Pt/C electrocatalysts were synthesized via the polyol method with ethylene glycol (EG) as reducing agent [28]. Separately, 80 mg of $C_{Ru\text{-dim}}$, $C_{Ru\text{-com}}$ or C were dispersed for 30 min by ultrasound in 48 mL of EG. The appropriate amount of $H_2PtCl_6 \cdot 6H_2O$ was dispersed in an ultrasonic bath for 30 min in 2 mL of EG and added to the Vulcan solution. The mixture was subjected to magnetic stirring for 1 h, followed by the adjustment of the pH to 12 by adding 2 mL of NaOH (1 mol L⁻¹). Then the temperature was increased to $130^\circ C$ under refluxing and stirring conditions, kept constant for 3 h and left to cool down to room temperature. Afterwards, 4 mL of H_2SO_4 (1 mol L⁻¹) were used to adjust the pH to 2, maintaining stirring for another 3 h. The solution was filtered and the dark powder obtained was washed and dried under vacuum atmosphere.

2.5. Physicochemical characterization

Nuclear Magnetic Resonance (NMR) analyses were obtained in a 500 MHz Bruker Advance III (using a 5 mm direct broad band with Z-grad (PABBO-1H/D Z-GRAD). The ¹H chemical shifts were referenced to residual no deuterated solvent. For $[(\eta^6-C_6H_5OCH_2CH_2OH)RuCl_2]_2$, ¹H-NMR (500 MHz, D_2O , δ ppm): 3.94 (t, 4 H, CH_2 , $J = 7.1$ Hz), 4.32 (t, 4 H, CH_2), 5.52 (m, 2 H, Ph), 5.54 (m, 4 H, Ph), 6.07 (t, 4 H, A Ph , $J = 9.2$ Hz).

Fourier Transformed Infrared spectra (FT-IR) were acquired using a Thermo-Nicolet 6700 spectrometer in the 4000–600 cm⁻¹ region, with a nominal resolution of 4 cm⁻¹ using the ATR technique. The experimental spectra were evaluated using the OMNIC

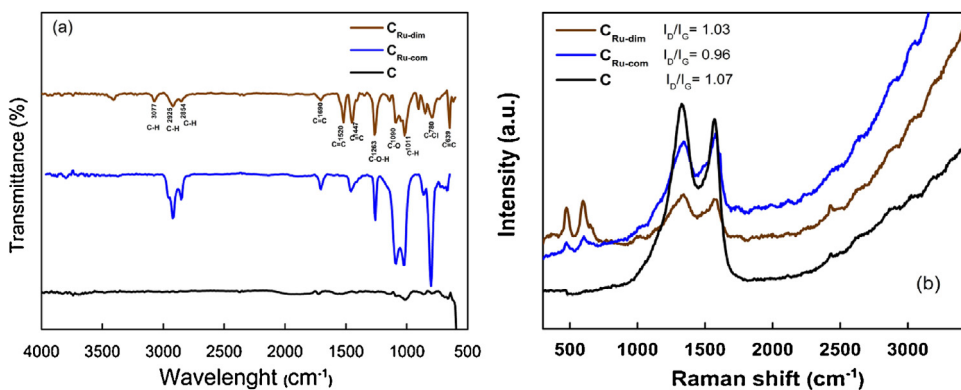


Fig. 1. a) FTIR and b) Raman spectra of CRu-dim, CRu-com and C.

software. Raman micro-analysis was performed in a confocal μ -Surf explorer microscope (Horiba) equipped with a 532 nm laser. The spectra were recorded over the 4000–400 cm⁻¹ range. X-Ray Diffraction (XRD) patterns were recorded in an Empyrean PANalytical diffractometer with a Bragg–Brentano geometry operated at 40 kV and 45 mA, using a Cu-K α radiation source ($\lambda = 1.5406 \text{ \AA}$) in the 2 θ range of 5–100° with a step scan of 0.0167 and 59 s per step.

The chemical composition of the carbon supports and the Pt electrocatalysts was determined in a Philips XL30 Scanning Electronic Microscope (SEM), equipped with the Energy Dispersive Spectroscopic (EDS) technique, under an accelerating voltage of 20 kV. The morphology of the supports was determined with the same apparatus.

The electrocatalysts were characterized by HR-TEM, HAADF-STEM and chemical mapping in a Jeol JEM-ARM200F microscope, operating at 30 kV. The chemical surface composition was studied by X-Ray Photoelectron Spectroscopy (XPS) in a Thermo Scientific Escalab 250 Xi instrument having an Al-K α (1486.68 eV) source and operating at ~ 10 mbar. The X-ray voltage and power were 14 kV and 350 W, respectively. The spectra were obtained using a pass energy of 20 eV. Peak fitting with Voight profiles was performed using the AAnalyzer software. The baseline corrections were made using the Shirley-Sherwood method. Binding energies were referenced to the C(1s) peak fixed at 284.8 eV.

2.6. Electrochemical characterization

Electrochemical measurements were carried out in a three-electrode electrochemical cell using a VoltaLab PGZ301 potentiostat/galvanostat. The counter-electrode was a Pt foil, while the reference electrode was of the Ag/AgCl type, although the potentials have been referred to the Standard Hydrogen Electrode (SHE). To build the thin-film working electrodes, a mirror-finished glassy carbon disk (5 mm diameter) was used. Catalytic inks were prepared by separately sonicating 10 mg of Pt/CRu-dim, Pt/CRu-com or Pt/C for 30 min, in a mixture containing 2 mL isopropyl alcohol and 5 μL Nafion solution. Then, aliquots of 10 μL of each electrocatalyst were deposited over the glassy carbon and let to dry.

Cyclic voltammograms (CVs) were acquired in N₂-saturated 0.5 mol L⁻¹ H₂SO₄, in the 0.05 to 1.2 V (vs. SHE) potential range, at a scan rate of 20 mV s⁻¹. The Electrochemically Active Surface Area (ECSA) of the electrocatalysts was determined from the H_{des} region. In order to evaluate their catalytic activity for the MOR, polarization curves were acquired in the same conditions, adding 0.5 mol L⁻¹ CH₃OH to the electrolyte. CO-stripping measurements were carried out bubbling CO into the cell for 10 min while polarizing the electrode at 0.075 V (vs. SHE), followed by Ar purging for 20 min.

Then, CVs were recorded at 20 mV s⁻¹ in the 0.05 to 1.2 V range (vs. SHE).

3. Results and discussion

3.1. Physicochemical characterization of the carbon supports

Fig. 1a shows the FT-IR spectra of CRu-dim, CRu-com and non-functionalized Vulcan (C). The latter displays weak bands in the 600–1690 cm⁻¹ range, attributed to the C–C, C–H and C–O vibrations of carbon [33,34]. On the other hand, the positive effect of functionalization is shown for CRu-dim and CRu-com. The intense absorption bands in the 3077–2854 and 1690–1477 cm⁻¹ intervals are attributed to C–H and C=C vibrations, respectively. It is worth noticing that CRu-dim displays a C=C band at 1520 cm⁻¹ not observed for CRu-com. Moreover, C–O–H, C–O and C–H signals are also observed [35,36]. At ca. 780 cm⁻¹, CRu-com shows a high-intensity band corresponding to C–Cl stretchings ascribed to the interactions of Vulcan and ruthenium chloride [37]. Thus, it is concluded that Ru-dim and Ru-com modify the surface characteristics of Vulcan, developing functional groups that promote the anchorage of Pt nanoparticles.

Fig. 1b shows the Raman spectra of CRu-dim, CRu-com and C. All the supports display the expected signals for carbon materials: i) the D band at ca. 1350 cm⁻¹ related to lattice disorder, attributed to the C–C vibrations of the sp³ defect sites; and ii) the G signal at ca. 1580 cm⁻¹ corresponding to sp² hybridization from C=C bonds (graphitized lattice), due to π interactions [38,39]. Additionally, two peaks at 604 and 466 cm⁻¹ assigned to ruthenium–carbon interphases, can be observed at CRu-dim and CRu-com, feature that correlates well with the reaction of ruthenium oxides and ruthenium crystals with organic molecules reported elsewhere [40,41].

The degree of hybridization due to a shift from sp² to sp³ orbitals can be determined from the ratio of the intensities of the D and G bands, I_D/I_G [42–45]. The ratios decrease from 1.07 for non-functionalized Vulcan, to 1.03 and 0.96 for CRu-dim and CRu-com, respectively. Based on this behavior, it can be concluded that the graphitized lattice of Vulcan is not distorted during the formulation of CRu-dim and CRu-com. To the best of our knowledge, organometallic surface modification of Vulcan has not been reported previously. However, the surface functionalization of carbon nanotubes and graphene with [(η^6 -C₆H₆)₂Cr] showed that bis-hexahapto-metal bonds are formed, preserving their graphitic band structure as reported elsewhere [46]. Based on the Raman spectra shown here, an analogous bonding can be proposed from the interaction of Ru complexes with graphitic Vulcan, based on the affinity of ruthenium atoms for aromatic rings. Such type of bond is strong, since the d orbitals of the transition metal couple with the π system of

Table 1

Chemical composition of $C_{Ru\text{-dim}}$ and $C_{Ru\text{-com}}$, from EDS analysis.

Support	C (wt.%)	Ru	O	Cl
$C_{Ru\text{-dim}}$	65.72	17.24	4.63	12.40
$C_{Ru\text{-com}}$	71.90	10.04	7.96	9.82

Vulcan, not modifying its band structure in what seems to be a constructive rehybridization [46].

Fig. 2 displays SEM images showing the morphology of a) Vulcan, with typical semi-spherical particles; b) $Ru\text{-dim}$, having large irregularly-shaped crystals; c) $C_{Ru\text{-dim}}$, which shows mixed features of Vulcan and $Ru\text{-dim}$; and d) $C_{Ru\text{-com}}$, also with semi-spherical particles larger than those of Vulcan, attributed to the treatment with $Ru\text{-com}$.

The chemical composition of the functionalized supports obtained from EDS analysis is shown in **Table 1**. Paying attention on Ru, both have considerably large contents, higher in the case of $C_{Ru\text{-dim}}$ than $C_{Ru\text{-com}}$ (17.24 and 10.04 wt.%, respectively). It is interesting to mention that such high amounts of Ru confirm the chemical stability of the $Ru\text{-dim}$ organometallic compound, since it remains on the surface of the carbon material after functionalization (seen also in **Fig. 2c**). Also, it is hypothesized that ruthenium atoms may be coordinated with carbon atoms on the graphitized segments of the lattice, although this should be confirmed with more studies of $C_{Ru\text{-dim}}$. Evidently, the carbon content has decreased as a result of the surface modification of Vulcan with $Ru\text{-dim}$ and $Ru\text{-com}$. The presence of O and Cl from the Ru chemical precursors is also reported in **Table 1**.

3.2. Physicochemical characterization of $Pt/C_{Ru\text{-dim}}$, $Pt/C_{Ru\text{-com}}$ and Pt/C

The XRD pattern of Pt/C in **Fig. 3a** shows the (111), (200), (220) and (311) reflections at 39.74° , 46.25° , 67.45° and 81.29° respectively (in 2θ scale), corresponding to fcc platinum (JCPDS 04-0802). A reflection at 24.92° , attributed to the (002) plane of carbon, is also observed. $Pt/C_{Ru\text{-com}}$ has the same Pt features, while $Pt/C_{Ru\text{-dim}}$ shows only the (111) and (311) Pt reflections. Two features attributed to the presence of Ru on the surface of the supports are observed for the patterns of $Pt/C_{Ru\text{-dim}}$ and $Pt/C_{Ru\text{-com}}$: i) the peak due to carbon is not evident; and ii) a peak at about 9° can be clearly seen. **Fig. 3b** shows the deconvolution of the diffraction peak at low angles observed for $Pt/C_{Ru\text{-dim}}$ and $Pt/C_{Ru\text{-com}}$. Three overlapped signals attributed to the (110), (101) and (102) ruthenium crystal planes (in 2θ positions of 7.6, 9.2 and 11.2, respectively) have been determined. This finding confirms that the reflection can be ascribed to Ru, in good agreement with the literature [5,47].

Fig. 3c shows the shift toward higher angles of the Pt (311) plane at $Pt/C_{Ru\text{-dim}}$ and $Pt/C_{Ru\text{-com}}$ relative to Pt/C . It is to be noticed that the displacement is almost 2° in the 2θ scale for $Pt/C_{Ru\text{-dim}}$ (**Table 2**), larger than those reported for Pt–Ru alloys synthesized by the polyol and other methods [48–51]. This is evidence that Pt nanoparticles and Ru atoms from the organometallic compound form Pt–Ru alloyed phases at $Pt/C_{Ru\text{-dim}}$. The same can be argued for $Pt/C_{Ru\text{-com}}$ since it also shows a shift in the (311) plane (**Table 2**).

To confirm this claim, the degree of alloying has been analyzed from the data of reflection (311). The lattice parameter (a_{fcc}) of $Pt/C_{Ru\text{-dim}}$, $Pt/C_{Ru\text{-com}}$ and Pt/C is determined according to the well-known equation (4), as reported elsewhere [52]:

$$a_{fcc} = \frac{\sqrt{2}\lambda_{\alpha_1}}{\sin \theta_{\max}} \quad (4)$$

where λ_{α_1} is the X-ray wavelength (1.54056 \AA) and θ_{\max} is the peak angle. Using Vegard's law [53], the atomic fraction of Ru alloyed (X_{Ru}) is calculated with Eq. (5) [54]:

$$a_{fcc} = l_{oc} - kX_{Ru} \quad (5)$$

where $l_{oc} = 3.9155 \text{ \AA}$ is the lattice parameter for pure platinum supported on carbon and $k = 0.124 \text{ \AA}$ is a constant. The values of a_{fcc} and X_{Ru} are given in **Table 2**. $Pt/C_{Ru\text{-dim}}$ and $Pt/C_{Ru\text{-com}}$ have a significant lattice contraction relative to Pt/C . Particularly, $Pt/C_{Ru\text{-dim}}$ shows the strongest reduction resulting in $a_{fcc} = 0.283 \text{ nm}$, which is smaller than the value reported for bulk Pt–Ru alloys [52]. Additionally, the atomic fraction of Ru alloyed on $Pt/C_{Ru\text{-dim}}$ and $Pt/C_{Ru\text{-com}}$ is approximately 50% higher than values reported for Pt–Ru/C alloys synthesized by some workers [15,51,54] and similar to a commercial Pt–Ru black [50]. Therefore, the experimental procedure is highly efficient to alloy Ru with Pt, reaching an important value starting from the $Ru\text{-dim}$:Vulcan molar ratio of 1:10 proposed here.

The crystallite size of the electrocatalysts (d) is calculated from the (311) diffraction peak using Scherrer's equation [55]:

$$d = \frac{0.9 \times \lambda_{\alpha_1}}{\beta_{2\theta} \times \cos \theta_{\max}} \quad (6)$$

where λ_{α_1} and θ_{\max} have the same meaning as in Eq. (1) and $\beta_{2\theta}$ is the full width at half maximum (FWHM) of the peak. The d values are given in **Table 2**. All the electrocatalysts show nanostructured characteristics, nevertheless, the smallest value is that of $Pt/C_{Ru\text{-dim}}$ (1.49 nm).

The chemical composition of the electrocatalysts (from EDS) is given in **Table 3**. Pt/C shows metal and carbon contents (18.07 and 81.93 wt.%, respectively) close to the nominal value of 20:80 (wt.%). On the other hand, $Pt/C_{Ru\text{-com}}$ and $Pt/C_{Ru\text{-dim}}$ have higher Pt content (23.68 and 26.82 wt.%, respectively). Interestingly, these two anodes have a significant amount of Ru, which in the case of $Pt/C_{Ru\text{-dim}}$ is three times higher (20.74 wt.%). Their carbon content has decreased significantly since Ru must be anchored on the surface of Vulcan, somehow hindering the support. The chemical composition analysis explains in part the fact that the C (002) peak is missing in the XRD profiles of $Pt/C_{Ru\text{-dim}}$ and $Pt/C_{Ru\text{-com}}$. Cl and O have also been detected for $Pt/C_{Ru\text{-dim}}$ and $Pt/C_{Ru\text{-com}}$. Both in **Table 1** and 2, the Cl content is higher in the presence of $Ru\text{-dim}$, which can be attributed to the larger Cl–Ru bonds at the organometallic structure, relative to $Ru\text{-com}$.

Fig. 4a shows the morphology of Pt/C , with platinum nanoparticles homogeneously dispersed over Vulcan. The histogram in **Fig. 4b** indicates that the average particle size (d) of Pt nanoparticles is 1.91 nm, in good agreement with the value determined from XRD analysis (**Table 2**). The nanostructured characteristic of Pt/C is observed more clearly in the HR-TEM micrograph of **Fig. 4c**, where the inset is a Selected Area Electron Diffraction (SAED) pattern with a distance between lattice fringes of 0.23 nm, attributed to Pt (111). On the other hand, the micrograph of $Pt/C_{Ru\text{-com}}$ in **Fig. 4d**

Table 2

Structural parameters of the electrocatalysts from the (311) Pt reflection.

Electrocatalyst	Peak position (°)	a_{fcc} (nm)	X_{Ru} (%)	d, XRD (nm)	d, TEM (nm)
Pt/C	81.22	0.398	–	2.05	1.91
$Pt/C_{Ru\text{-com}}$	82.37	0.331	0.489	1.89	1.87
$Pt/C_{Ru\text{-dim}}$	83.13	0.283	0.509	1.49	2.59

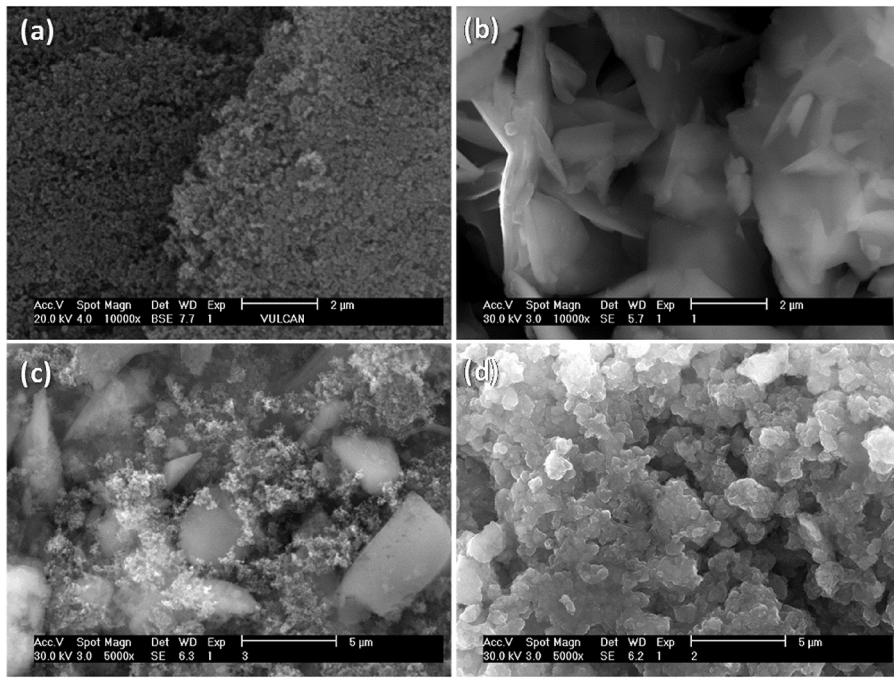


Fig. 2. SEM micrographs of: a) C, b) Ru-dim, c) C_{Ru-dim} and d) C_{Ru-com}.

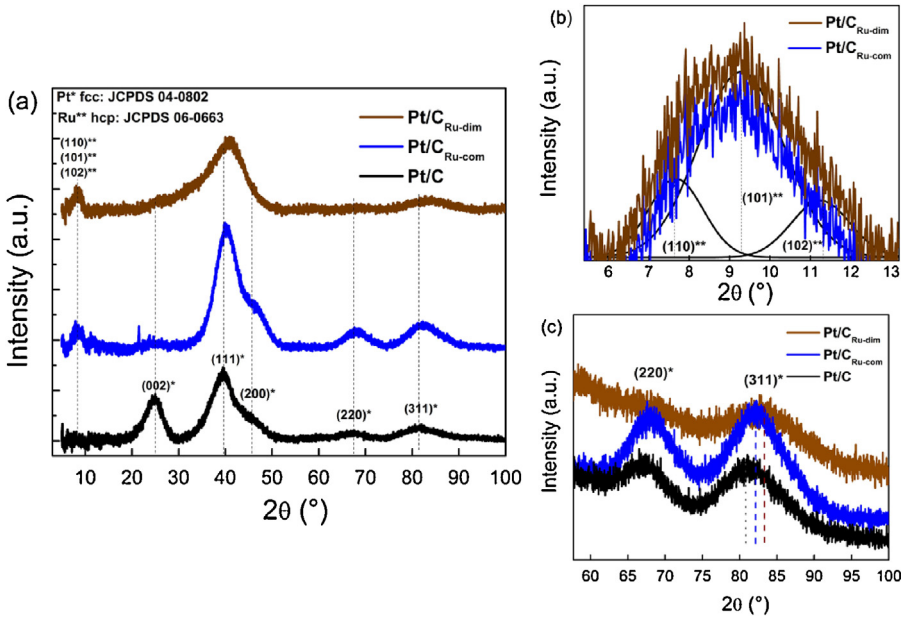


Fig. 3. (a) XRD patterns of Pt/C_{Ru-dim}, Pt/C_{Ru-com} and Pt/C. (b) Zooming of the 5–13° (2θ) range. (c) Zooming of the (220) and (311) Pt reflections.

Table 3

Chemical composition from EDS analysis and ECSA values of the electrocatalysts.

Electrocatalyst	C (wt.%)	Pt	Ru	Cl	O	ECSA (m ² g _{Pt} ⁻¹)
Pt/C	81.93	18.07	–	–	–	47.75
Pt/C _{Ru-com}	57.56	23.68	7.68	0.54	10.54	41.90
Pt/C _{Ru-dim}	42.64	26.82	20.74	1.17	8.62	47.27

shows that Pt nanoparticles are homogeneously dispersed over the entire surface of C_{Ru-com}. The d value from the histogram in Fig. 4e is 1.87 nm, basically the same as that from XRD (Table 2). Fig. 4f is a HR-TEM image of Pt/C_{Ru-com}. From the SAED pattern in the inset, distances between lattice fringes of 0.23 and 0.20 nm have

been obtained and ascribed to Pt (111) and Ru (101), respectively [56–59].

Fig. 5a is a TEM micrograph of Pt/C_{Ru-dim}, showing that the support is more densely covered by metallic nanoparticles than in the case of Pt/C and Pt/C_{Ru-com}. Fig. 5b is the corresponding

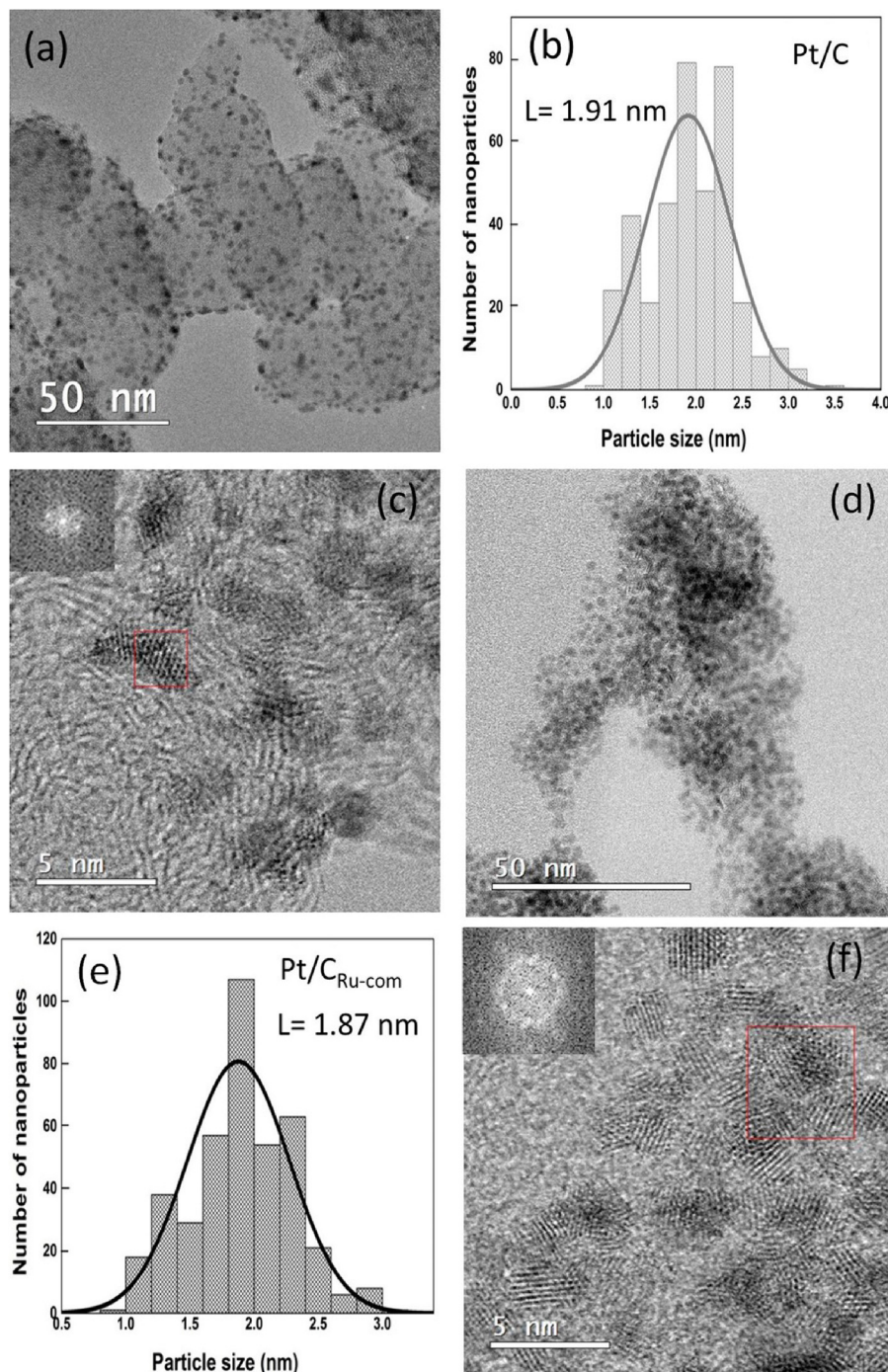


Fig. 4. TEM micrograph, histogram and HRTEM image of Pt/C (a–c) and Pt/C_{魯-com} (d–f). SAED patterns from the regions in the red squares are shown in the insets.

histogram indicating that $d = 2.29$ nm (Table 2). The larger value compared to that determined from XRD can be in part due to the fact that the nanoparticles actually touch each other, avoiding a clear delimitation of their boundaries. Even though, such d value confirms the nanostructured nature of the Pt metallic nanoparticles anchored over C_{魯-dim}. The elemental mapping in STEM mode (Fig. 5c) confirms the presence of Pt and Ru, and demonstrates that both metals are homogeneously dispersed over the support. Fig. 5d is a HR-TEM image of Pt/C_{魯-dim}, where the SAED pattern allows the determination of distances between lattice fringes of 0.23 and 0.20 nm, attributed also to Pt (111) and Ru (101) respectively [56–59].

Fig. 6a shows the C1s spectrum for Pt/C, where the most intense signal is that of carbon sp² hybridization at a binding energy (BE) of 284.1 eV. The smaller C sp³ peak emerges at higher BE.

As previously reported in the literature for Carbon Nanotubes and Graphene [46], Ru atoms may bond with graphitic carbon via hexahapto coordination of the ($\eta^6\text{-C}_6\text{H}_6\text{-M}$) type, preserving the sp² hybridization. Fig. 6b and c are the C1s and Ru3d spectra for Pt/C_{魯-dim} and Pt/C_{魯-com}, respectively, showing significant differences compared to Pt/C. The C1s BE overlaps with the Ru3d region, as seen by the presence of Ru 3d_{5/2} and Ru 3d_{3/2} doublets of metallic Ru and RuO₂, Ru⁰ and Ru^{IV}, respectively. Pt/C_{魯-dim} shows a decrease in the relative intensities of C sp² and sp³ (compared to Pt/C) and higher peaks attributed to the Ru⁰ doublet. Its Ru^{IV} dou-

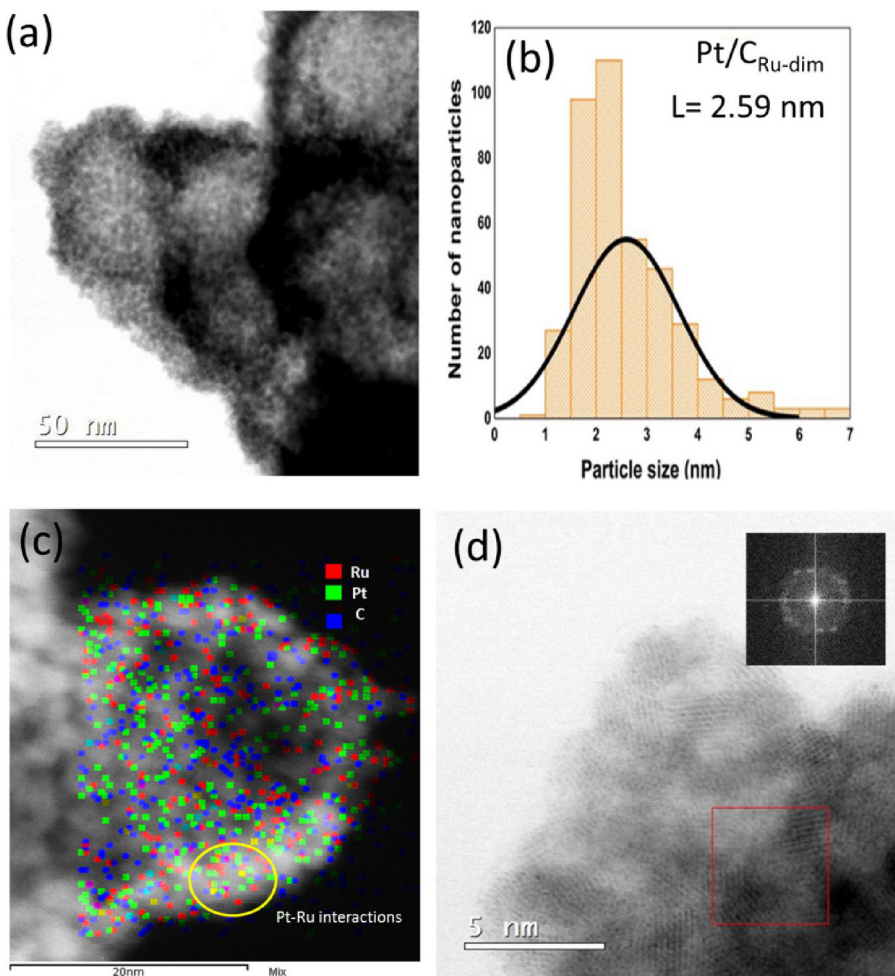


Fig. 5. Analysis of Pt/C_{Ru-dim}: (a) TEM micrograph, (b) Histogram of particle distribution, (c) Elemental mapping and (d) HRTEM image. SAED pattern from the region in the red square is shown in the inset.

blet is less intense if compared with the metallic contribution. On the other hand, the highest peak for Pt/C_{Ru-com} is that of C sp², with the Ru⁰ and Ru^{IV} doublets as well as C sp³ showing lower relative intensities. Even more, Fig. 6d and e show the doublets due to Ru and RuO₂ in the Ru3p BE region. Pt/C_{Ru-dim} has higher relative intensities of the Ru 3p_{3/2} and Ru 3p_{1/2} peaks compared to Pt/C_{Ru-com}, indicating a larger ruthenium concentration.

Fig. 7a-c show the Pt 4f BE region for the electrocatalysts, with doublets from the spin-orbit splitting of the 4f_{7/2} and 4f_{5/2} states due to metallic Pt and PtO (Pt⁰ and Pt^{II}, respectively). The Pt spin-orbit splittings are larger on Pt/C_{Ru-dim} (3.40 and 3.45 eV), followed by Pt/C_{Ru-com} (3.28 and 3.31 eV) and Pt/C (3.26 and 3.24 eV), as given in Table 4. Also, the BE of Pt⁰ in the 4f_{7/2} state is shifted from 71.31 eV in the case of Pt/C, to 71.63 and 71.50 eV for Pt/C_{Ru-dim} (0.32 eV displacement) and Pt/C_{Ru-com} (0.19 eV displacement), respectively. The electronic modification of Pt/C_{Ru-dim} and Pt/C_{Ru-com} corresponds to a change of the d-valence band of Pt, attributed to an electron transfer from Ru to Pt atoms, and clearly suggests the formation of Pt–Ru alloyed phases. A similar behavior is pointed out by Watanabe *et al.* [60] where the core level of Pt 4f_{7/2} associated to a Pt–Ru alloy has been observed to shift 0.39 eV to higher BE with respect to that for pure Pt, due to differences in their work functions. Therefore, shift in BE of Pt/C_{Ru-dim} is close to the one reported in [60].

Moreover, the spin-orbit splittings of Ru 3p_{3/2} and Ru 3p_{1/2} are also given in Table 4. The values are larger for Pt/C_{Ru-com} compared to Pt/C_{Ru-dim}. On the other hand, the analysis of the O1s core level

region in Fig. 7d-f corroborates the existence of PtO and C=O bonds on Pt/C. Besides that, RuO₂ bonds are observed for Pt/C_{Ru-dim} and Pt/C_{Ru-com}.

The XPS chemical composition of the electrocatalysts is presented in Table 4. The C sp² content is 78.82, 9.39 and 35.4 (at.%) for Pt/C, Pt/C_{Ru-dim} and Pt/C_{Ru-com}, respectively. This result showing a lower C content at Pt/C_{Ru-dim} and Pt/C_{Ru-com} can be related to the significant presence of Ru after functionalization of Vulcan (Table 3). In the case of the Pt⁰ and Pt^{II} species, Pt/C_{Ru-com} shows the larger concentration, followed by Pt/C_{Ru-dim}. Nevertheless, it should be pointed out that Pt/C_{Ru-dim} has higher Ru⁰ and RuO₂ content than Pt/C_{Ru-com}. The relevant role of RuO₂ on the catalytic activity of Pt–Ru/C alloys for the Ethanol Oxidation Reaction has been determined elsewhere [61], at which an increased performance compared to Pt/C was attributed to an easier oxygen transfer at more negative potentials. The RuO₂ species may also be important in the catalytic activity for the MOR, as discussed later in this work.

3.3. Catalytic activity of Pt/C_{Ru-dim}, Pt/C_{Ru-com} and Pt/C for the MOR

The CVs of the electrocatalysts in Fig. 8 show with the characteristic regions of platinum materials: i) hydrogen adsorption and desorption (H_{ads/des}) in the potential range of 50–250 mV vs. SHE; ii) double layer (250–700 mV vs. SHE); iii) Pt-oxides formation/reduction (700–1200 mV vs. SHE). The shape of Pt/C is that of a monometallic supported electrocatalysts [62,63], with 3 H_{des}

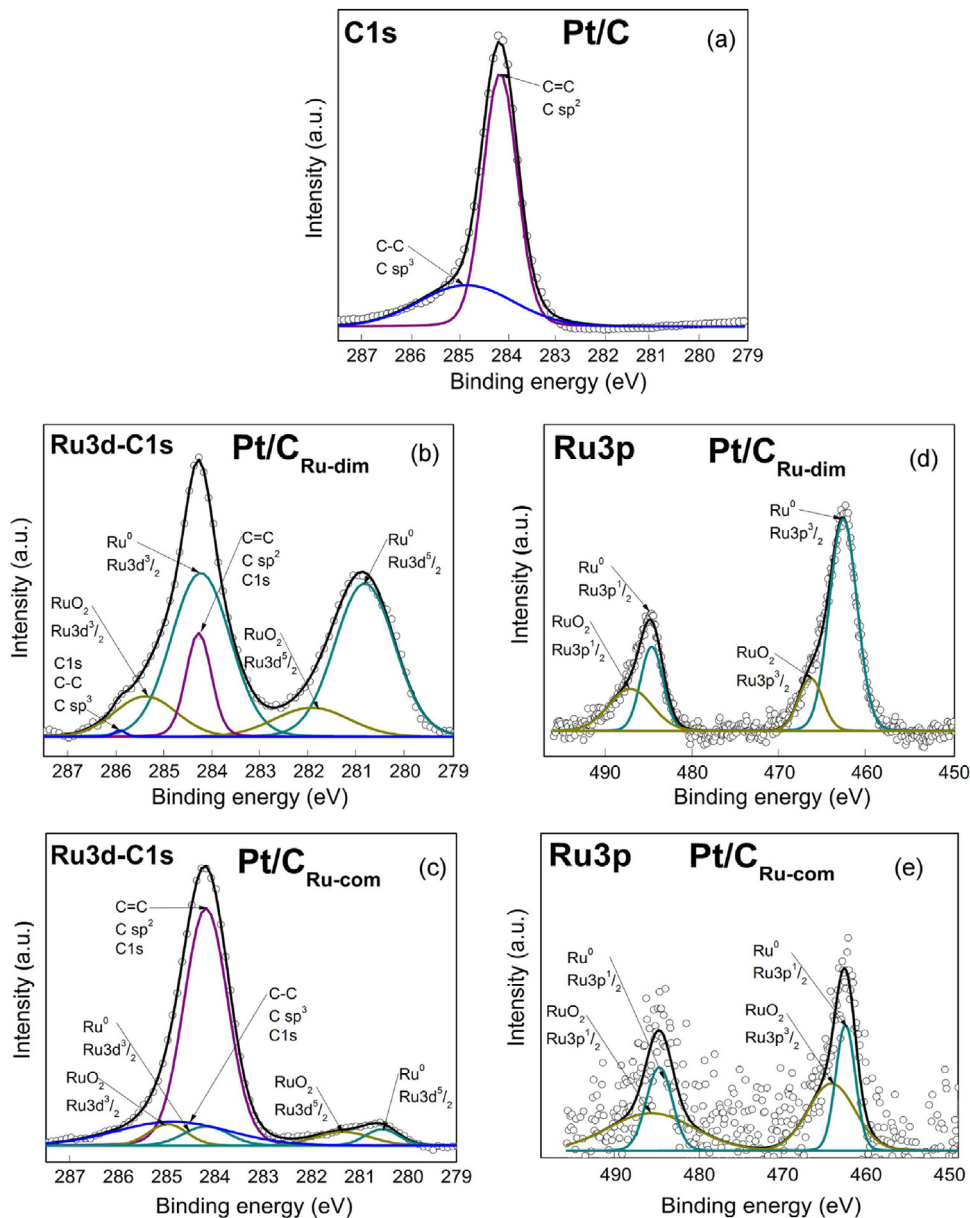


Fig. 6. XPS spectra of the electrocatalysts: a) C1s region of Pt/C, b-c) Overlapped Ru3d-C1s regions of Pt/C_{Ru-dim} and Pt/C_{Ru-com}, d-e) Ru3p region of Pt/C_{Ru-dim} and Pt/C_{Ru-com}.

peaks identified. It also has a relatively thin double layer with the current density in the positive scan parallel to the zero current line. Moreover, the onset potential of the Pt-oxides formation and the peak current density due to their reduction are distinguishable.

Pt/C_{Ru-dim} and Pt/C_{Ru-com} show some differences relative to Pt/C. The hydrogen peaks are hindered and the double layer region is wider, exposing a current density slope up to the Pt-oxides region. Due to this feature, the onset potential of the oxides formation is not detected. Similar characteristics are attributed to the presence of Ru and the formation of RuOH species on Pt-Ru/C alloys [63] and suggest the formation of alloyed Pt-Ru at Pt/C_{Ru-dim} and Pt/C_{Ru-com} in accordance with their XRD, TEM and XPS characterization.

The electrochemically active surface area (ECSA, in $\text{m}^2 \text{ g}_{\text{Pt}}^{-1}$) is calculated from the H_{des} region of the CVs in Fig. 8 (after correction the corresponding area related to the double layer) with Eq. (4):

$$\text{ECSA} = \frac{Q}{Q_{H_{\text{des}}} \times L_{\text{Pt}}} \quad (4)$$

where Q is the charge under the curve (μC), $Q_{H_{\text{des}}}$ is the theoretical charge due to the adsorption of hydrogen on Pt ($210 \mu\text{C cm}^{-2}$) and L_{Pt} (μg) is the amount of Pt on the electrodes obtained from the chemical composition. The ECSA value of Pt/C_{Ru-dim} is similar to that of Pt/C (47.75 and $47.27 \text{ m}^2 \text{ g}_{\text{Pt}}^{-1}$, respectively) and higher than the $41.90 \text{ m}^2 \text{ g}_{\text{Pt}}^{-1}$ determined for Pt/C_{Ru-com} (Table 3).

The catalytic activity of the electrocatalysts for the MOR is shown in the polarization curves of Fig. 9a). Pt/C_{Ru-dim} delivers a current density (j_{geo} , considering the geometrical area of the glassy carbon electrode) of 45.0 mA cm^{-2} , an almost two-fold increase compared to Pt/C and Pt/C_{Ru-com} (Table 5). Moreover, plots of the performance in terms of mass catalytic activity, taking into account the Pt mass content on each electrocatalyst from EDS analysis, are shown in Fig. 9b). Pt/C_{Ru-dim} generates a mass current density (j_{mass}) of $344.2 \text{ mA mg}_{\text{Pt}}^{-1}$, a value roughly 1.3 and 1.6 higher than Pt/C and Pt/C_{Ru-com}, respectively. Therefore, the enhanced catalytic activity of Pt/C_{Ru-dim} for the MOR is demonstrated in Fig. 9a and b. Its mass performance is highlighted because Pt/C shows a higher mass catalytic activity than Pt/C_{Ru-com}, indicating that the Ru

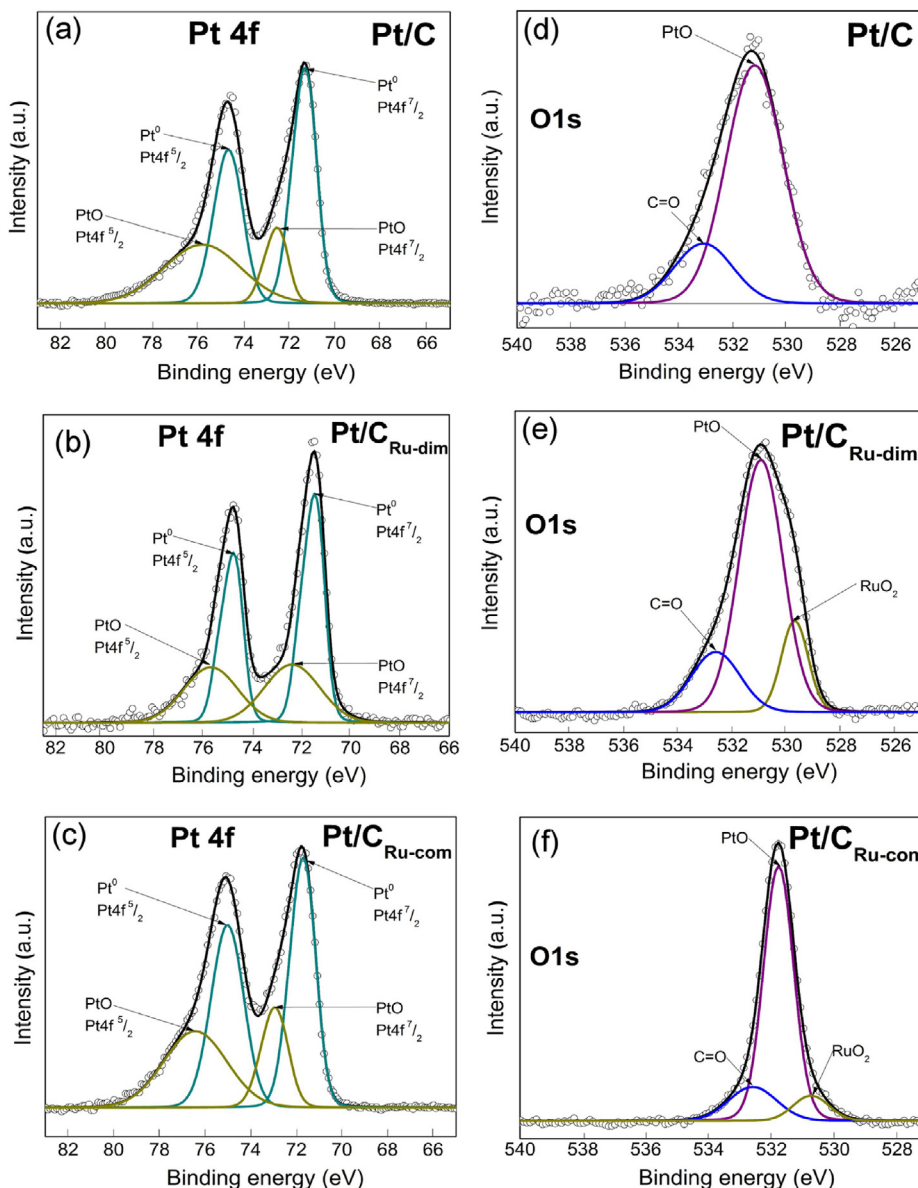


Fig. 7. XPS spectra of Pt/C, Pt/C_{Ru-dim} and Pt/C_{Ru-com}: a-c) Pt 4f region, d-f) O1s region.

organometallic compound interacts with Pt nanoparticles to promote the MOR more efficiently than the Ruthenium chloride salt. The onset potential of the MOR (E_{onset}) at Pt/C_{Ru-dim} is 0.25 mV, significantly more negative than the values determined for Pt/C_{Ru-com} and Pt/C (0.35 and 0.39 mV, respectively). Moreover, the current density ratios in the forward and the backward scan (j_f/j_b), are 1.3, 1.3 and 0.8 for Pt/C_{Ru-dim}, Pt/C_{Ru-com} and Pt/C, respectively. Therefore, the Ru-containing electrocatalysts are more efficient for the oxidation of methanol with low formation of intermediates. The electrochemical parameters given in Table 5, demonstrate the enhanced catalytic activity of Pt/C_{Ru-dim} for the MOR compared to the two other anodes. Overall, the catalytic activity decreases in the order Pt/C_{Ru-dim} > Pt/C_{Ru-com} > Pt/C.

Even though experimental conditions may differ (methanol concentration, electrolyte, scan rate, carbon support, metal loading, plot vs. reference electrode), a comparison of the catalytic activity of Pt/C_{Ru-dim} for the MOR with some reports in the literature can be attempted. By comparing j_{mass} with Pt-Ru electrocatalysts under a scan rate of 20 mV s^{-1} during the CV, it is observed that the electrochemical parameters of the MOR in Table 5 show that

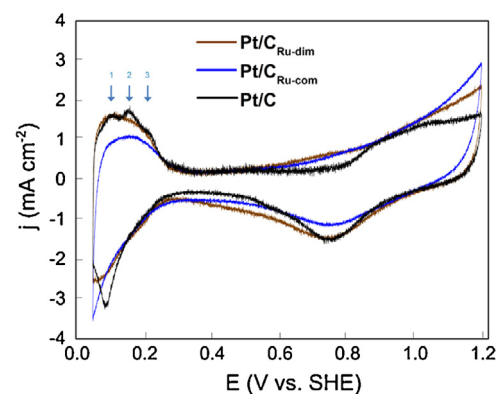


Fig. 8. CVs of Pt/C, Pt/C_{Ru-dim} and Pt/C_{Ru-com} in Ar-saturated 0.5 M H₂SO₄. Scan rate: 20 mV s⁻¹.

Table 4

XPS parameters of the electrocatalysts.

Electrocatalyst	Species	State	BE (eV)	Doublet splitting (eV)	Composition (at.%)
Pt/C	Pt ⁰	Pt 4f _{7/2}	71.31	3.26	3.53
		Pt 4f _{5/2}	74.57		3.76
	PtO	Pt 4f _{7/2}	72.57	3.24	2.74
		Pt 4f _{5/2}	75.81		1.50
	C sp ²	O1s	531.23		7.65
		C1s	284.15		78.82
		O1s	532.70		1.97
Pt/C _{Ru-dim}	Pt ⁰	Pt 4f _{7/2}	71.63	3.40	4.64
		Pt 4f _{5/2}	75.03		5.86
	PtO	Pt 4f _{7/2}	72.94	3.45	1.94
		Pt 4f _{5/2}	76.39		4.73
	Ru ⁰	O1s	530.95		31.04
		Ru3p _{3/2}	466.45	20.82	10.93
		Ru3p _{1/2}	487.27		7.04
	RuO ₂	Ru3p _{3/2}	462.78	21.89	2.39
		Ru3p _{1/2}	484.67		6.79
		O1s	529.72		6.96
	C sp ²	C1s	284.29		9.39
		O1s	532.62		8.24
Pt/C _{Ru-com}	Pt ⁰	Pt 4f _{7/2}	71.50	3.28	6.34
		Pt 4f _{5/2}	74.78		6.74
	PtO	Pt 4f _{7/2}	72.38	3.31	4.93
		Pt 4f _{5/2}	75.69		2.69
	Ru ⁰	O1s	531.78		28.41
		Ru3p _{3/2}	464.14	21.85	0.93
		Ru3p _{1/2}	485.99		1.64
	RuO ₂	Ru3p _{3/2}	462.50	22.35	1.19
		Ru3p _{1/2}	484.85		2.44
		O1s	530.72		3.31
	C sp ²	C1s	284.19		35.40
		O1s	532.59		5.94

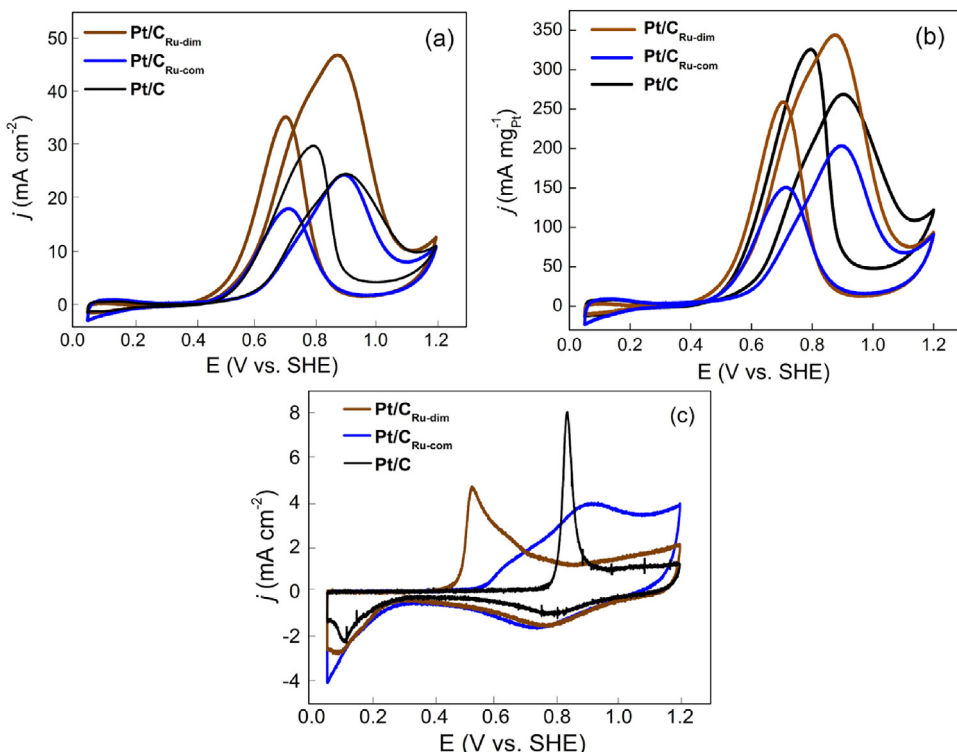


Fig. 9. a) CVs of the MOR at Pt/C_{Ru-dim}, Pt/C_{Ru-com} and Pt/C, considering the geometrical area of the glassy carbon electrode. b) Mass catalytic activity of Pt/C_{Ru-dim}, Pt/C_{Ru-com} and Pt/C, taking into account the Pt content at each electrocatalyst (from EDS analysis). Electrolyte: Ar-saturated 0.5 M H₂SO₄ + 0.5 M CH₃OH. Scan rate: 20 mV s⁻¹. c) CO-stripping curves of the electrocatalysts in 0.5 M H₂SO₄ at the same scan rate.

Table 5

Electrochemical parameters for Pt/C_{Ru-dim}, Pt/C_{Ru-com} and Pt/C during the MOR and the CO-stripping evaluation.

Electrocatalyst	MOR				CO-stripping		
	j_{geo} (mA cm ⁻²)	j_{mass} (mA mg _{Pt} ⁻¹)	E_{onset} (V)	j_f/j_b ratio	j (mA cm ⁻²)	E_{onset} (V)	E_{max} (V)
Pt/C	24.6	269.7	0.39	0.8	8.0	0.76	0.83
Pt/C _{Ru-com}	24.5	203.8	0.35	1.3	—	0.53	—
Pt/C _{Ru-dim}	45.0	344.2	0.25	1.3	4.7	0.43	0.52

Pt/C_{Ru-dim} delivers a higher j_{mass} than that reported by Ren and Xing with a PtRu/CNT catalyst and 2.0 M CH₃OH [10]. The j_{mass} value of Pt/C_{Ru-dim} is of the same order as that shown in the work by Sun et al. with a commercial 40 wt.% Pt/XC-72 [48], even though it can be highlighted that j_b is clearly smaller in the case of this work. Even more, the mass current density of Pt/C_{Ru-dim} is higher than those of Pt-Ru/XC-72 electrocatalysts also reported in [48] with 1 M CH₃OH. Xin et al. evaluated a series of PtRu/C electrodes in 0.5 M CH₃OH/0.5 M H₂SO₄ electrolyte [50], which generated smaller j_{mass} than Pt/C_{Ru-dim} here (even though, the j_b of those electrocatalysts is significantly low). Pt/C_{Ru-dim} also shows a higher j_{mass} in terms of Pt content than a PtRu/GS-CNT tested by Hu et al. with 1 M CH₃OH (even though, the j_f/j_b ratio of the alloys on the porous support is very high) [64].

It is well-known that CO_{ads} is produced as intermediate species during the MOR, poisoning and limiting the catalytic activity of Pt-alone nanomaterials [1,2]. Therefore, anode electrocatalysts for DMFCs must fulfill the requirement of high tolerance to such species. Pt-Ru/C alloys are highly active for the MOR in part because of the bifunctional mechanism, since the formation of (OH)_{ads} species starts earlier on Ru than on Pt [65].

Fig. 9c depicts the electrochemical response of Pt/C_{Ru-dim}, Pt/C_{Ru-com} and Pt/C during CO-stripping measurements. The latter shows a narrow CO oxidation peak with $E_{\text{onset}} = 0.76$ V, $j = 8.0$ mA cm⁻² and a maximum j value at $E_{\text{max}} = 0.83$ V (Table 5). Meanwhile, on the Pt/C_{Ru-com} and Pt/C_{Ru-dim} electrocatalysts the CO oxidation proceeds in a different fashion, with remarkably broad peaks. It is interesting to observe the formation of two peaks (at ca. 0.65 V and 0.90 V) on Pt/C_{Ru-com}, indicating the oxidation of two CO-like species adsorbed on Pt sites at different energies. This electrocatalyst oxidizes CO with $E_{\text{onset}} = 0.53$ V, a value more negative than that of Pt/C.

On the other hand, it is worth noticing the behavior to Pt/C_{Ru-dim}, at which the CO oxidation reaction starts at $E_{\text{onset}} = 0.43$ V, i.e., 320 mV more negative than Pt/C. Moreover, $j = 4.7$ mA cm⁻² and $E_{\text{max}} = 0.52$ V at this electrocatalyst (Table 5). A peak at ca. 0.65 V is also observed, similar to the CO-like species indicated for Pt/C_{Ru-com} at the same potential. This result indicates that CO_{ads} is more weakly adsorbed on Pt/C_{Ru-dim} and therefore can be oxidized at lower potentials relative to Pt/C_{Ru-com} and Pt/C.

Here, it is proposed that the bifunctional mechanism (reactions 1–3) proceeds on Pt/C_{Ru-dim} during the MOR, i.e., (OH)_{ads} species are formed on the Ru sites generated from the organometallic compound at low potentials and transferred to the Pt atoms. As a consequence, the oxidation of CO_{ads} is highly improved, thus enhancing its catalytic activity for the MOR. Also, the catalytic behavior of Pt/C_{Ru-dim} for the MOR can be attributed to the ligand effect. The shift in BE due to the electronic effect of Ru on Pt observed from XPS analysis indicates a weaker adsorption of CO-like species at the electrocatalyst [61], i.e., it can be oxidized at lower potentials, in agreement with the results in Fig. 9b. Even more, the high RuO₂ content at Pt/C_{Ru-dim} may have played a beneficial role on its high performance for the MOR.

In summary, Pt/C_{Ru-dim} shows enhanced catalytic properties as anode material for DMFCs applications. An excellent review of the development of DMFCs is reported in [66]. Several researchers have designed DMFCs stacks with active or passive configurations,

operating with diluted or concentrated methanol. Moreover, industrial laboratories have developed DMFCs for portable, stationary and miniature-power devices applications [66]. It is proposed that Pt/C_{Ru-dim} can be evaluated in such type of devices.

4. Conclusions

Vulcan was functionalized with the [(η⁶-C₆H₅OCH₂CH₂OH)RuCl₂]₂ organometallic compound to produce C_{Ru-dim}, having several functional groups as identified by FTIR. Raman analysis revealed an apparent chemical interaction between ruthenium and the graphitic phase of Vulcan, maintaining the sp² hybridization typical of ordered carbon.

Pt/C_{Ru-dim} showed physicochemical characteristics that strongly suggest the formation of alloyed Pt-Ru phases.

- From XRD: shift in diffraction peaks, presence of reflections attributed to Ru, contraction of a_{fcc} and nearly 50% X_{Ru}.
- From TEM: chemical mapping showing the homogeneous dispersion of Pt and Ru nanoparticles, and identification of distances between lattice fringes ascribed to Pt and Ru.
- From XPS: The identification of Ru⁰ and RuO₂ bonds, besides those of Pt⁰ and PtO. A shift to higher BE of Pt⁰ in the 4f_{7/2} state.

Pt/C_{Ru-dim} showed a higher catalytic activity for the MOR considering the j_{geo} , j_{mass} , E_{onset} and j_f/j_b values. It also demonstrated a significant increased tolerance to CO_{ads} relative to Pt/C_{Ru-com} and Pt/C. The electrocatalytic behavior of Pt/C_{Ru-dim} was attributed to the bifunctional mechanism, the ligand effect and the presence of RuO₂.

The physicochemical characteristics and excellent electrochemical response of the novel Pt/C_{Ru-dim} for the MOR opens the opportunity for the design of electrocatalysts for specific fuel cell reactions, employing organometallic compounds as agents for functionalization. For example: Pt/C_{Sn} for the ethanol oxidation reaction or Pt/C_M (where M = Co, Fe, Ni, etc.) for the Oxygen Reduction Reaction. The potential application is also there for other carbonaceous supports, such as Graphene, Carbon Nanotubes and Ordered Mesoporous Carbon, instead of Vulcan.

Acknowledgements

This work was financially supported by the Mexican National Council for Science and Technology (CONACYT) through grant 241526. AASC thanks CONACYT for doctoral scholarship. The authors thank R. Rangel (CIQA) for FT-IR and Raman measurements.

References

- [1] H.R. Corti, E.R. Gonzalez, Direct Alcohol Fuel Cells Materials Performance, Durability and Applications, Springer Science, New York, USA, 2014.
- [2] E.R. Gonzalez, A. Mota-Lima, in: H.R. Corti, E.R. Gonzalez (Eds.), Direct Alcohol Fuel Cells Materials Performance, Durability and Applications, Springer Science, New York, USA, 2014, p. 33.
- [3] P. Waszczuk, J. Solla-Gullón, H.-S. Kim, Y.Y. Tong, V. Montiel, A. Aldaz, A. Wieckowski, Methanol electrooxidation on platinum/ruthenium nanoparticle catalysts, *J. Catal.* 203 (2001) 1–6.

[4] A.S. Arico, P.L. Antonucci, E. Modica, V. Baglio, H. Kim, V. Antonucci, Effect of Pt–Ru alloy composition on high-temperature methanol electro-oxidation, *Electrochim. Acta* 47 (2002) 3723–3732.

[5] Y.-C. Hsieh, Y. Zhang, D. Su, V. Volkov, R. Si, L. Wu, Y. Zhu, W. An, P. Liu, P. He, S. Ye, R.R. Adzic, J.X. Wang, Ordered bilayer ruthenium–platinum core-shell nanoparticles as carbon monoxide-tolerant fuel cell catalysts, *Nat. Commun.* 4 (2013), article number: 2466.

[6] M. Marques-Tusi, N. Soares-Polanco, M. Brandalise, O. Vercino-Correa, J.C. Villalba, F. Jacó-Anaissi, A. Oliveira-Neto, E. Vitorio-Spinacé, PtRu/carbon hybrids with different Pt:Ru atomic ratios prepared by hydrothermal carbonization for methanol electro-oxidation, *Int. J. Electrochem. Sci.* 6 (2011) 484–491.

[7] H. Liu, Ch. Song, L. Zhang, J. Zhang, H. Wang, D.P. Wilkinson, A review of anode catalysis in the direct methanol fuel cell, *J. Power Sources* 155 (2006) 95–110.

[8] T. Maiyalagan, T.O. Alaje, K. Scott, Highly stable Pt–Ru nanoparticles supported on three-dimensional cubic ordered mesoporous carbon (Pt–Ru/CMK-8) as promising electrocatalysts for methanol oxidation, *J. Phys. Chem. C* 116 (2012) 2630–2638.

[9] J.R.C. Salgado, F. Alcaide, G. Álvarez, L. Calvillo, M.J. Lázaro, E.J. Pastor, Pt–Ru electrocatalysts supported on ordered mesoporous carbon for direct methanol fuel cell, *J. Power Sources* 195 (2010) 4022–4029.

[10] L. Ren, Y. Xing, Effect of pH on PtRu electrocatalysts prepared via a polyol process on carbon nanotubes, *Electrochim. Acta* 53 (2008) 5563–5568.

[11] S. Yang, Ch. Zhao, Ch. Ge, X. Dong, X. Liu, Y. Liu, Y. Fang, H. Wang, Z.J. Li, Ternary Pt–Ru–SnO₂ hybrid architectures: unique carbon-mediated 1-D configuration and their electrocatalytic activity to methanol oxidation, *Mater. Chem.* 22 (2012) 7104–7107.

[12] E. Antolini, Carbon supports for low-temperature fuel cell catalysts, *Appl. Catal. B: Environ.* 88 (2009) 1–25.

[13] L. Calvillo, M.J. Lázaro, E. García-Bordejé, R. Moliner, P.L. Cabot, I. Esparbé, E. Pastor, J.J. Quintana, Platinum supported on functionalized ordered mesoporous carbon as electrocatalyst for direct methanol fuel cells, *J. Power Sources* 169 (2007) 59–64.

[14] A. Capelo, M.A. Esteves, A.I. de Sá, R.A. Silva, L. Cangueiro, A. Almeida, R. Vilar, C.M. Rangel, Stability and durability under potential cycling of Pt/C catalyst with new surface-functionalized carbon support, *Int. J. Hydrogen Energy* 41 (2016) 12962–12975.

[15] J.R.C. Salgado, R.G. Duarte, L.M. Ilharco, A.M. Botelho do Rego, A.M. Ferraria, M.G.S. Ferreira, Effect of functionalized carbon as Pt electrocatalyst support on the methanol oxidation reaction, *Appl. Catal. B: Environ.* 102 (2011) 496–504.

[16] J.R.C. Salgado, J.C.S. Fernandes, A.M. Botelho do Rego, A.M. Ferraria, R.G. Duarte, M.G.S. Ferreira, Pt–Ru nanoparticles supported on functionalized carbon as electrocatalysts for the methanol oxidation, *Electrochim. Acta* 56 (2011) 8509–8518.

[17] D. Morales-Acosta, F.J. Rodríguez-Varela, R. Benavides, Template-free synthesis of ordered mesoporous carbon: application as support of highly active Pt nanoparticles for the oxidation of organic fuels, *Int. J. Hydrogen Energy* 41 (2016) 3387–3398.

[18] Ch. Yu-Chun, L. Chia-Chun, Ch. Chun-Ping, Characterization of platinum nanoparticles deposited on functionalized graphene sheets, *Materials* 8 (2015) 6484–6497.

[19] M. Lütfi Yola, T. Eren, N. Atar, H. Saral, Í. Ermiş, Direct-methanol fuel cell based on functionalized graphene oxide with mono-metallic and Bi-metallic nanoparticles: electrochemical performances of nanomaterials for methanol oxidation, *Electroanalysis* 28 (2016) 570–579.

[20] W.J. Pech-Rodríguez, D. González-Quijano, G. Vargas-Gutiérrez, J.I. Escalante-García, F.J. Rodríguez-Varela, Electrochemical characterization of Pt nanocatalysts supported on functionalized Vulcan XC-72 for the EOR, *ECS Transactions* 61 (2014) 11–18.

[21] S.S. Rich, J.J. Burk, Ch.S. Kong, C.D. Cooper, D.E. Morse, Nitrogen functionalized carbon black: A support for Pt nanoparticle catalysts with narrow size dispersion and high surface area, *Carbon* 81 (2015) 115–123.

[22] H. Wang, Q. Ma, Selenium and oxygen-containing functional groups for co-functionalization of Vulcan carbon and its applications in ethanol oxidation, *J. Solid State Electrochem.* 19 (2015) 355–360.

[23] A. Eguizabal, L. Uson, V. Sebastian, J.L. Hueso, M.P. Pina, Efficient and facile tuning of Vulcan XC72 with ultra-small Pt nanoparticles for electrocatalytic applications, *RSC Adv.* 5 (2015) 90691–90697.

[24] N. Jha, P. Ramesh, E. Belyarova, X. Tian, F. Wang, M.E. Itkis, R.C. Haddon, Functionalized single-walled carbon nanotube-based fuel cell benchmarked against US DOE 2017 technical targets, *Sci. Rep.* 3 (2013), article number: 2257.

[25] J. Soleimannejad, C. White, A convenient one-pot synthesis of a functionalized-arene ruthenium half-sandwich compound [$\text{RuCl}_2(\eta^6\text{-C}_6\text{H}_5\text{OCH}_2\text{CH}_2\text{OH})_2$], *Organometallics* 24 (2005) 2538–2541.

[26] S. Sarkar, S. Niyogi, E. Belyarova, R.C. Haddon, Organometallic chemistry of extended periodical π-electron systems: hexahapto-chromium complexes of graphene and single-walled carbon nanotubes, *Chem. Sci.* 2 (2011) 1326–1333.

[27] E. Belyarova, S. Sarkar, S. Niyogi, R.C. Haddon, Advances in the chemical modification of epitaxial graphene, *J. Phys. D: Appl. Phys.* 45 (2012), article number: 154009.

[28] D. González-Quijano, W.J. Pech-Rodríguez, J.I. Escalante-García, G. Vargas-Gutiérrez, F.J. Rodríguez-Varela, Electrocatalysts for ethanol and ethylene glicol oxidation reactions. Part I: Effects of the polyol synthesis conditions on the characteristics and catalytic activity of PtSn/C anodes, *Int. J. Hydrogen Energy* 39 (2014) 16676–16685.

[29] M.E. Tess, P.L. Hill, K.E. Torracca, M.E. Kerr, K.A. Abboud, L. McElwee-White, Bimetallic Pt/Ru complexes as catalysts for the electrooxidation of methanol, *Inorg. Chem.* 39 (2000) 3942–3944.

[30] M. Bevilacqua, C. Bianchini, A. Marchionni, J. Filippi, A. Lavacchi, H. Miller, W. Oberhauser, F. Vizza, G. Granozzi, L. Artiglia, S.P. Annen, F. Krumelich, H. Grützmacher, Improvement in the efficiency of an OrganoMetallic Fuel Cell by tuning the molecular architecture of the anode electrocatalyst and the nature of the carbon support, *Energy Environ. Sci.* 5 (2012) 8608–8620.

[31] S.P. Annen, V. Bambagioni, M. Bevilacqua, J. Filippi, A. Marchionni, W. Oberhauser, H. Schönberg, F. Vizza, C. Bianchini, H. Grützmacher, A biologically inspired organometallic fuel cell (OMFC) that converts renewable alcohols into energy and chemicals, *Angew. Chem. Int. Ed.* 49 (2010) 7229–7233.

[32] R.C. Haddon, S. Sarkar, S. Niyogi, E. Belyarova, M.E. Itkis, X. Tian, F. Wang, U.S. Patent, 0202515, 2013.

[33] V. Tucoreanu, A. Matei, A.M. Avram, *Crit. Rev. Anal. Chem.* 2016, 0, DOI: 10.1080/10408347.2016.1157013.

[34] F. Rositani, P.L. Antonucci, M. Minutoli, N. Giordano, Infrared analysis of carbon blacks, *Carbon* 25 (1987) 325–332.

[35] S. Wang, D. Yu, L. Dai, D.W. Chang, J.-B. Baek, Polyelectrolyte-functionalized graphene as metal-free electrocatalysts for oxygen reduction, *ACS Nano* 5 (2011) 6202–6209.

[36] G. Selvarani, A.K. Sahu, N.A. Choudhury, P. Sridhar, S. Pitchumani, A.K. Shukla, A phenyl-sulfonic acid anchored carbon-supported platinum catalyst for polymer electrolyte fuel cell electrodes, *Electrochim. Acta* 52 (2007) 4871–4877.

[37] R.M. Silverstein, F.X. Webster, D.J. Kiemle, *Spectrometric Identification of Organic Compounds*, 7th ed., John Wiley & Sons Inc, Hoboken, NJ, USA, 2005.

[38] M.S. Dresselhaus, A. Jorio, A.G. Souza-Filho, R. Saito, Defect characterization in graphene and carbon nanotubes using Raman spectroscopy, *Phil. Trans. R. Soc. A* 368 (2010) 5355–5377.

[39] A.C. Ferrari, Raman spectroscopy of graphene and graphite: disorder, electron–phonon coupling, doping and nonadiabatic effects, *Solid State Commun.* 143 (2007) 47–57.

[40] A.-X. Yin, W.-Ch. Liu, J. Ke, W. Zhu, J. Gu, Y.-W. Zhang, Ch.-H. Yan, Ru nanocrystals with shape-dependent surface-enhanced raman spectra and catalytic properties: controlled synthesis and DFT calculations, *J. Am. Chem. Soc.* 134 (2012) 20479–20489.

[41] H. Kim, B.N. Popov, Characterization of hydrous ruthenium oxide/carbon nanocomposite supercapacitors prepared by a colloidal method, *J. Power Sources* 104 (2002) 52–61.

[42] D. Akbar, Ü.E. Güngör, Determination of the incorporation rate of PTFE particles in Au-Co-PTFE composite coatings by InfraRed Reflection Absorption Spectroscopy, *Surf. Coat. Technol.* 240 (2014) 233–241.

[43] M.A. Pimenta, G. Dresselhaus, M.S. Dresselhaus, L.G. Cancado, A. Jorio, R. Saito, Studying disorder in graphite-based systems by Raman spectroscopy, *Phys. Chem. Chem. Phys.* 9 (2007) 1276–1290.

[44] S. Sarkar, H. Zhang, J.-W. Huang, F. Wang, E. Belyarova, C.N. Lau, R.C. Haddon, Organometallic hexahapto functionalization of single layer graphene as a route to high mobility graphene devices, *Adv. Mater.* 25 (2012) 1131–1136.

[45] Z. Tang, L. Zhang, Ch. Zeng, T. Lin, B. Guo, General route to graphene with liquid-like behavior by non-covalent modification, *Soft Matter* 8 (2012) 9214–9220.

[46] E. Belyarova, S. Sarkar, F. Wang, M.E. Itkis, I. Kalinina, X. Tian, R.C. Haddon, Effect of covalent chemistry on the electronic structure and properties of carbon nanotubes and graphene, *Acc. Chem. Res.* 46 (2013) 65–76.

[47] Y. Yang, Ch. Sun, Y. Ren, S. Hao, D. Jiang, New route toward building active ruthenium nanoparticles on ordered mesoporous carbons with extremely high stability, *Sci. Rep.* 4 (2013), article number: 4540.

[48] J. Guo, G. Sun, S. Sun, S. Yan, W. Yang, J. Qi, Y. Yan, Q. Xin, Polyol-synthesized PtRu/C and PtRu black for direct methanol fuel cells, *J. Power Sources* 168 (2007) 299–306.

[49] Z. Liu, X.Y. Ling, X. Su, J.Y. Lee, L.M. Gan, Preparation and characterization of Pt/C and Pt–Ru/C electrocatalysts for direct ethanol fuel cells, *J. Power Sources* 149 (2005) 1–7.

[50] L. Jiang, G. Sun, X. Zhao, Z. Zhou, S. Yan, S. Tang, G. Wang, B. Zhou, Q. Xin, Preparation of supported PtRu/C electrocatalyst for direct methanol fuel cells, *Electrochim. Acta* 50 (2005) 2371–2376.

[51] Y. Chen, Y. Zhou, Y. Tang, T. Lu, Electrocatalytic properties of carbon-supported Pt–Ru catalysts with the high alloying degree for formic acid electrooxidation, *J. Power Sources* 195 (2010) 4129–4134.

[52] V. Radmilovic, H.A. Gasteiger, P.N. Ross, Structure and chemical composition of a supported Pt–Ru electrocatalyst for methanol oxidation, *J. Catal.* 154 (1995) 98–106.

[53] G.S. Chai, S.B. Yoon, J.-S. Yu, J.-H. Choi, Y.-E. Sung, Ordered porous carbons with tunable pore sizes as catalyst supports in direct methanol fuel cell, *J. Phys. Chem. B* 108 (2004) 7074–7079.

[54] J.W. Guo, T.S. Zhao, J. Prabhuram, R. Chen, C.W. Wong, Preparation and characterization of a PtRu/C nanocatalyst for direct methanol fuel cells, *Electrochim. Acta* 51 (2005) 754–763.

[55] G. Liu, H. Zhang, J. Hu, Novel synthesis of a highly active carbon-supported $\text{R}_{0.8}\text{Se}_{1.5}$ chalcogenide catalyst for the oxygen reduction reaction, *Electrochim. Commun.* 9 (2007) 2643–2648.

[56] N.M. Sánchez-Padilla, S.M. Montemayor, L.A. Torres, F.J. Rodríguez-Varela, Fast synthesis and electrocatalytic activity of M@Pt (M = Ru, Fe₃O₄, Pd) core-shell nanostructures for the oxidation of ethanol and methanol, *Int. J. Hydrogen Energy* 38 (2013) 12681–12688.

[57] N.M. Sánchez-Padilla, D. Morales-Acosta, M.D. Morales-Acosta, S.M. Montemayor, F.J. Rodríguez-Varela, Catalytic activity and selectivity for the ORR of rapidly synthesized M@Pt (M = Pd, Fe₃O₄, Ru) core-shell nanostructures, *Int. J. Hydrogen Energy* 39 (2014) 16706–16714.

[58] S. Agarwal, J.N. Ganguli, Hydrogenation by nanoscale ruthenium embedded into the nanopores of K-10 clay, *RSC Adv.* 4 (2014) 11893–11898.

[59] W. Chen, D. Ghosh, J. Sun, M.C. Tong, F. Deng, S. Chen, Dithiocarbamate-protected ruthenium nanoparticles: synthesis, spectroscopy, electrochemistry and STM studies, *Electrochim. Acta* 53 (2007) 1150–1156.

[60] M. Wakisaka, S. Mitsui, Y. Hirose, K. Kawashima, H. Uchida, M. Watanabe, Electronic structures of Pt–Co and Pt–Ru alloys for CO-tolerant anode catalysts in polymer electrolyte fuel cells studied by EC–XPS, *J. Phys. Chem. B* 110 (2006) 23489–23496.

[61] J. Datta, S. Sen Gupta, S. Singh, S. Mukherjee, M. Mukherjee, Significant role of Ru-oxide present in the Pt–Ru alloy catalyst for ethanol electro-oxidation in acid medium, *Mater. Manuf. Processes* 26 (2011) 261–271.

[62] F.J. Rodríguez Varela, O. Savadogo, Catalytic activity of carbon-supported electrocatalysts for direct ethanol fuel cell applications, *J. Electrochem. Soc.* 155 (2008) B618–B624.

[63] D.C. Azevedo, W.H. Lizcano-Valbuena, E.R. Gonzalez, An impedance study of the rate determining step for methanol oxidation on platinum and platinum-ruthenium supported on high surface area carbon, *J. New. Mat. Electrochem. Syst.* 7 (2004) 191–196.

[64] Yu-Sheng Wang, Shin-Yi Yang, Shin-Ming Li, Hsi-Wen Tien, Sheng-Tsung Hsiao, Wei-Hao Liao, Chia-Hong Liu, Kuo-Hsin Chang, Chen-Chi M. Ma, Chi-Chang Hu, Three-dimensionally porous graphene–carbon nanotube composite-supported PtRu catalysts with an ultrahigh electrocatalytic activity for methanol oxidation, *Electrochim. Acta* 87 (2013) 261–269.

[65] E. Ticanelli, J.G. Beery, M.T. Paffett, S. Gottesfeld, An electrochemical, ellipsometric, and surface science investigation of the PtRu bulk alloy surface, *J. Electroanal. Chem. Interfacial Electrochem.* 258 (1989) 61–77.

[66] Xianglin Li, Amir Faghri, Review and advances of direct methanol fuel cells (DMFCs) part I: Design, fabrication, and testing with high concentration methanol solutions, *J. Power Sources* 226 (2013) 223–240.